

Rubrene vs. fluorinated-functionalized rubrene molecules: self-assembly, electronic structure and energy alignment

Jonathan Viereck, Sylvie Rangan, and Robert A. Bartynski

Department of Physics and Astronomy and Laboratory for Surface Modification, Rutgers University, Piscataway, USA

Patricio Haberle

Departamento de Física, Universidad Tecnica Federico Santa Maria, Valparaiso, Chile

Elena Galoppini

Department of Chemistry, Rutgers University, Newark, USA

Christopher J. Douglas

Department of Chemistry, University of Minnesota, Minneapolis, USA

(Dated: July 3, 2018)

The influence of fluorine-functionalization of the rubrene molecule is explored by comparing rubrene and a fluorinated rubrene (FM-rubrene), adsorbed on a Ag(100) surface. The self-assembly, studied using scanning tunneling microscopy, reveals highly ordered molecular assemblies at the monolayer level, that are incompatible with epitaxial growth of rubrene or FM-rubrene ordered crystals. Moreover, the molecular order has a direct influence on the resulting electronic structure and energy alignment of the molecular levels with the band edges of Ag(100), measured using UV and inverse photoemission spectroscopies. A careful comparison of the adsorption of rubrene and FM-rubrene on Ag(100) enables a fundamental understanding of the molecular-surface and inter-molecular interactions, as well as their effects on molecular crystal growth and energy alignment with supporting surfaces.

I. INTRODUCTION

Rubrene (5,6,11,12-tetraphenyltetracene) has attracted considerable attention in the last 20 years as a benchmark organic semiconductor with an outstanding hole mobility of $30 \text{ cm}^2 \text{ V}^{-1} \text{ s}^{-1}$ in its crystalline form¹. This has led to the fabrication of single crystal organic field effect transistors (sc-OFETs) with world-record performance²⁻⁶. Such facile charge transport is believed to arise from favorable overlap of the π -systems on the tetracene backbones of neighboring molecules^{7,8}. The electron mobility of rubrene, on the other hand, is relatively low, leading to recent efforts to search for rubrene derivatives with increased electron mobility and with a goal of achieving high performance ambipolar charge transport for switchable OFETs. A promising candidate that has emerged is bis(trifluoromethyl)-dimethyl-rubrene, referred to in the literature as FM-rubrene^{9,10}. In this molecule, phenyls 5 and 11 have methyl pendent groups in the para position, while phenyls 6 and 12 have instead para trifluoromethyl groups. The increased hydrogen bonding due to the presence of $-\text{CF}_3$ groups has been shown to increase the hole mobility¹¹. Fabricating a sc-OFET using carbon nanotubes as the electrodes, has yielded record ambipolar mobilities of $4.8 \text{ cm}^2 \text{ V}^{-1} \text{ s}^{-1}$ for hole transport and $4.2 \text{ cm}^2 \text{ V}^{-1} \text{ s}^{-1}$ for electron transport¹².

Although there has been a significant effort to study the charge transport properties in bulk crystals of these materials, forming interfaces between thin crystalline films and other materials, such as metals or semicon-

ductors, has been challenging. Rubrene possesses a flat tetracene backbone in its crystal form. In contrast, when rubrene adsorbs on a wide range of surfaces, near edge adsorption spectroscopy (NEXAFS) experiments indicate that the molecule adopts a conformation with a twisted tetracene backbone, similar to its gas phase conformation.¹³ It was proposed that this conformational mismatch is the reason why growth of epitaxial rubrene on top of an adsorbed rubrene monolayer is not possible, thus explaining why only polycrystalline thin films are obtained on most surfaces.¹³ Scanning tunneling microscopy studies of rubrene adsorption hint at similar conclusions, although most studies were performed at low temperature and sometimes with limited resolution.¹⁴⁻¹⁹ However, progress towards growing more ordered rubrene thin films has been made using as substrates organic single crystals²⁰⁻²³, selected organic buffer layers²⁴⁻²⁷, hexagonal boron nitride (h-BN)²⁸ or a Bi(001) surface²⁹. While the understanding of ordered rubrene growth is limited, even less is known about the packing of fluorine-functionalized rubrene molecules on surfaces. In fact, only recently have bulk crystal structures been determined.^{9,10} The bulk molecular packing in single crystals of fluorine functionalized rubrene has been studied using X-ray diffraction and the tetracene packing upon molecular functionalization was related to charge transport properties.^{9,10} Moreover, previous work with polyaromatic fluorinated molecules suggests that additional interactions such as F-H hydrogen bonds will stabilize alternative structures on surfaces.³⁰⁻³²

From an electronic structure point of view, the occupied band structure of single crystal rubrene has

been studied using angle resolved photoemission spectroscopy.^{33,34} The thickness-dependence of the occupied and unoccupied electronic states of rubrene has been measured for polycrystalline thin films on several metal surfaces^{33,35,36}, as well as on H-terminated Si(100) and on a SiO₂/Si(100) thin dielectric.³⁵ Emphasis was placed on measuring work function changes and the interface dipole that develops upon rubrene deposition.^{33,35,36} A comparison of the energy level alignment of hydrogenated vs. fully or partially fluorinated rubrene monolayers on the Ag(111) and Au(111) surfaces suggested the possible influence of the partially fluorinated molecules dipole moment on the molecular packing at the metal surfaces.³⁷ However, none of these electronic structure studies were supplemented by local probes or geometric information about the rubrene/surface interface.

In this paper, we describe a series of scanning tunneling microscopy (STM), ultraviolet photoemission spectroscopy (UPS) and inverse photoemission spectroscopy (IPS) measurements of monolayers of rubrene and FM-rubrene on the Ag(100) surface, with emphasis on understanding both the rules directing self-assembly of these molecules on a model surface, and the consequences of rubrene functionalization on the electronic structure at the interface. High resolution STM images obtained at room temperature for a monolayer of these molecules indicate long range molecular order, but with unit cells that are incompatible with crystalline phase growth. The remarkable order of the FM-rubrene overlayer, along with the intrinsic dipole moment of each molecule, leads to the formation of a dipole layer that shifts the electronic levels of additional layers upwards in energy by 0.2 eV.

II. EXPERIMENTAL

A. Scanning Tunneling Microscopy.

STM measurements were performed in ultrahigh vacuum (UHV) at pressures better than 5×10^{-10} Torr with an Omicron variable temperature STM. The STM chamber was equipped with an argon ion sputtering source and a heater mounted to the manipulator arm in contact with the sample, permitting *in situ* preparation of the surface. Clean and atomically flat Ag(100) single crystal surfaces were achieved by performing cycles of argon-ion sputtering (3 μ A and 1.5 kV for 30 min) and annealing (500 °C for 30 min). The STM tip was electrochemically etched from tungsten wire. The images presented here were obtained in constant-current mode with the sample at room temperature. Rubrene molecules [Aldrich, $\geq 98\%$ purity] and custom synthesized FM-rubrene molecules^{9,10} were deposited by sublimation in the same UHV environment using a Knudsen cell held around 215 °C that was thoroughly outgassed prior to deposition. The deposition rate was determined from the STM measurements, which were processed using the WSxM software³⁸. In this work, one monolayer coverage is defined as saturation coverage

of the substrate surface by adsorbed molecules, as viewed in the STM. Subsequently, XPS measurements (Al K- α , Phi 15-255G CMA) were performed in the same system, in order to help calibrating deposition rates in the other spectroscopic studies.

For the STM measurements, because of a combination of noise and drift during imaging, the uncertainties were conservatively estimated to be ± 0.1 Å for heights, ± 0.5 Å for lateral distances, and 3° for angles.

The STM chamber is also equipped with a low-energy electron diffraction (LEED) system, with which the substrate surface high-symmetry directions can be determined. Alternatively, the Ag lattice can be imaged under particular conditions as explained below. High symmetry directions were subsequently used to orient molecular features to the substrate atomic rows.

B. Spectroscopic methods.

The electron spectroscopic measurements presented herein were obtained using a single UHV experimental chamber that housed instruments for X-ray and ultraviolet photoemission spectroscopies (XPS and UPS), as well as inverse photoemission spectroscopy (IPS), described in detail elsewhere³⁹. The base pressure of the chamber was less than 5×10^{-10} Torr. Valence band photoelectrons were excited using a Leybold-Heraeus helium discharge photon source (HeII: 40.8 eV), and core levels were probed using the nonmonochromated Al K α line of a SPECS XR50 dual anode source. The energy analysis of the emitted electrons was performed in an angle-integrated mode using a double-pass Phi 15-255G cylindrical mirror analyzer (CMA). The axes of the photon sources and the CMA formed a 90° angle, and the sample normal was oriented midway between the two.

Inverse photoemission spectra were obtained using a grating spectrometer, described in detail elsewhere⁴⁰, that was mounted on the same experimental chamber. Briefly, a well-collimated, monoenergetic electron beam (primary energy E_p , of 20.3 eV in this study) was directed toward the sample along the surface normal. The electrons coupled to high-lying unoccupied states, and a subset relaxed by way of a direct optical transition to low-lying unoccupied states in the conduction band, emitting a photon in the process. The photons were dispersed by a concave, spherical diffraction grating and detected by a microchannel plate with a position-sensitive resistive-anode encoder. With this approach, the intensity of the photons as a function of photon energy reflects the density of occupied states in the conduction band. In the photoemission and inverse photoemission spectra, occupied and unoccupied states were measured with respect to the Fermi level of the Ag substrate. The overall energy resolutions [full width at half-maximum (FWHM)] for the UPS and IPS spectra are estimated to be better than 0.3 and 0.6 eV, respectively.

In order to prevent electron beam damage, IPS mea-

measurements were recorded while maintaining a small sample current (0.5-1.0 μA) for a beam size of 1 nm^2 and by sampling several spots on a large 1 cm^2 sample with a short beam exposure (a few minutes). For such electron doses, no beam damage was observed during IPS or subsequent UPS and XPS analyses.

Surface adsorbate coverage in the photoemission chamber was determined by comparison with XPS spectra taken in the STM chamber of monolayer coverage for the two molecules. The rubrene and FM-rubrene films were grown starting from a pristine Ag(100) surface (checked with XPS) for each coverage.

C. Computational methods.

Electronic structure calculations were performed with the GAMESS(US) software package using the Becke three-parameter exchange functional and the Lee-Yang-Parr correlation functional (B3LYP) density functional theory (DFT) method. Geometries of local minima on the potential energy surface were calculated with Pople's 6-31G basis set for hydrogen, carbon, and fluorine. Molecular dimensions are computed from the largest H-H distance in a particular direction. The density of states (DOS) was obtained as a sum of individual electronic states convolved with a 0.7 FWHM Gaussian function⁴¹.

III. RESULTS AND DISCUSSION

A. Surface self-assembly and bulk properties

Although a large body of work has explored the possibility of growing rubrene compounds epitaxially on surfaces, using atomic force microscopy or different spectroscopic methods¹³⁻²⁹, very little information is available on the detailed self-assembly of rubrene or rubrene-derivatives at the molecular level at room temperature.

Figure 1 shows STM images of 1 ML film of rubrene adsorbed on the Ag(100) surface, along with a model of the molecule. Upon deposition at room temperature on this surface, rubrene assembles into a highly-ordered monolayer, characterized by a rhomboid unit cell, as shown in Figure 1 a). The contribution from individual rubrene molecules is easily identifiable as seen in Figure 1 b), and is composed of a vertical elongated center-part corresponding to the tetracene backbone, surrounded by four protrusions attributed to the phenyl moieties. The contrast among sub-molecular features can be related to the molecular conformation illustrated in Figure 1 c). Naturally occurring rubrene can be found in either of two symmetries as shown in Figures S1 a) and b) of the Supplemental Material. In its crystalline form, rubrene possesses a flat tetracene backbone and offset phenyls which reduces Coulomb repulsion. In the gas phase, the tetracene backbone is twisted along its longer dimension,

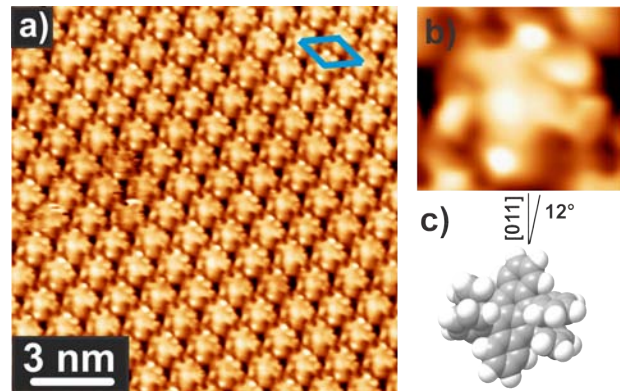


FIG. 1. a) Room temperature STM image of 1ML rubrene as deposited on Ag(100), taken at +0.6 V bias, and thus tunnelling into unoccupied states. b) Zoomed in view of a single rubrene molecule depicting intramolecular structure and (c) a space filling model of the gas-phase rubrene molecule oriented the same way as the molecule in b). Image information: $15 \times 15\text{ nm}^2$, $I = 0.3\text{ nA}$.

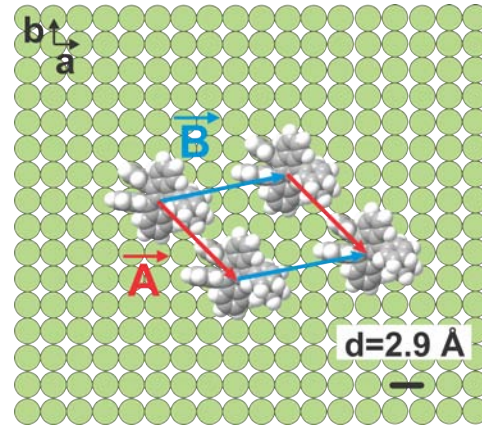


FIG. 2. Binding model for one monolayer rubrene on Ag(100), determined from the STM data of Figure 1. The lengths of the vectors **A** and **B** are 12.3 \AA and 14.8 \AA , respectively. Green circles represent surface Ag atoms, which have spacing 2.9 \AA . **a** and **b** are in the direction of vectors $[011]$ and $[01\bar{1}]$, respectively.

and the phenyls have an even a larger offset, as shown in Figure 3 c) resulting in the opposite phenyls assuming different heights. From these STM measurements, it is clear that upon adsorption on Ag(100), the opposite phenyls are significantly offset, as found in the gas phase configuration, suggesting a distorted tetracene backbone, consistent with earlier studies using NEXAFS spectroscopy.¹³

More information can be gathered by overlaying the unit cell of the measured rubrene array onto the Ag(100) lattice, as shown in Figure 2. The orientation of the substrate lattice was determined two ways: by imaging the Ag(100) substrate below the rubrene overlayer at low enough biases so as to avoid molecular states (as shown in Figure S3 of the Supplemental Materials), and by means

of low energy electron diffraction. Knowing the low index directions of the underlying surface, we can measure an angle of 12° between the long axis of the tetracene backbone and the $[011]$ direction of the Ag surface. The molecular lattice, defined by the vectors \mathbf{A} and \mathbf{B} is described by the matrix equation

$$\begin{pmatrix} \mathbf{A} \\ \mathbf{B} \end{pmatrix} = \begin{pmatrix} 3 & -3 \\ 5 & 1 \end{pmatrix} \begin{pmatrix} \mathbf{a} \\ \mathbf{b} \end{pmatrix} \quad (1)$$

where the \mathbf{a} and \mathbf{b} vectors are in the $[011]$ and $[01\bar{1}]$ directions, respectively. As the exact position of the rubrene molecule with respect to the Ag lattice was not resolved experimentally, rubrene molecules tentatively have been centered on Ag atop sites. Propagating the rubrene overlayer unit cell over the Ag(100) lattice leads to all rubrene molecules centered on atop sites, as seen in Figure 2. The dimensions for \mathbf{A} and \mathbf{B} are, 12.3 \AA and 14.8 \AA , respectively, leading to a surface area for the unit cell of 151.4 \AA^2 . The resulting packing density for this binding model is 6.6×10^{13} molecules per cm^2 . Note that, given the packing density of the rubrene overlayer, individual molecules would overlap if they were to lie flat on the surface. Rather, they are tilted with respect to the surface plane, with one side of the tetracene backbone raised above the Ag surface as shown in Figure 2. This geometry is supported in part by STM images obtained at different biases, as shown in Figure S4 of the Supplemental Material, which indicate a clear asymmetry of the tetracene backbone, with one end elevated with respect to the other. The adsorption geometry determined for rubrene on Ag(100), will be further compared to single crystal rubrene properties in the following section. It is important to point out that, while molecular multilayers would form at room temperature, it was not possible to obtain stable STM images for molecular exposures greater than one monolayer, implying a lack of order and high molecular mobility for molecules above the first monolayer.

As expected, partial fluorination of rubrene, drastically influences the molecular arrangement upon self-assembly. Figure 3 shows STM images and a model of the molecule for a monolayer of FM-rubrene adsorbed on the Ag(100) surface. As shown in Figure 3 a), the molecular layer has a nearly rectangular unit cell containing two molecules. Here again, contributions from individual FM-rubrene molecules can be isolated as shown in Figure 3 b), and compared to the gas phase model for FM-rubrene of Figure 3 c). Note that in both the gas phase and in crystalline form, an FM-rubrene conformation where its tetracene backbone is planar, as shown in Figure S1, is energetically favored. In Figure 3 b) the tetracene backbone is nearly aligned with $[011]$ direction of the Ag(100) surface, and is surrounded by two large protrusions and two smaller features, on opposite sides on the tetracene backbone, attributed to the phenyl- CF_3 groups and phenyl- CH_3 moieties, respectively. When considering the molecular ordering of Figure 3 a), one can observe that all molecules are oriented in the same

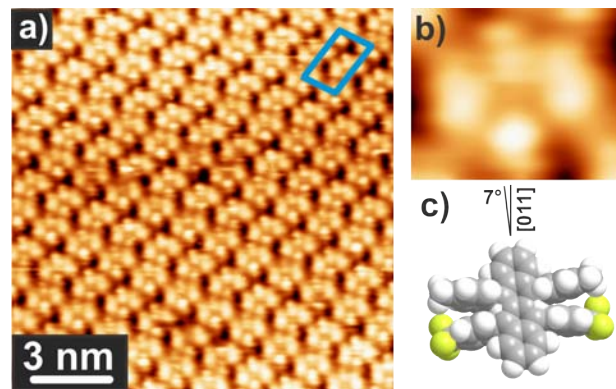


FIG. 3. (a) Room temperature STM image of an FM-rubrene monolayer as deposited on Ag(100), taken at 2.0 V bias. (b) Zoomed in image of a single FM-rubrene molecule showing three bright spots corresponding to the $-\text{CF}_3$ on both sides of the tetracene backbone and (c) a space-filling model of the gas phase FM-rubrene molecule in oriented identically to (b). Image information: $15 \times 15 \text{ nm}^2$, $I = 0.3 \text{ nA}$.

direction, leading to an alternation of the $-\text{CF}_3$ and $-\text{CH}_3$ groups. This arrangement minimizes the electrostatic energy of the positively charged $-\text{CH}_3$ and negatively charged $-\text{CF}_3$ groups.

Placing the FM-rubrene overlayer in registry with the Ag(100) lattice, it is found that each tetracene backbone makes an angle of 7° with respect to the $[011]$ crystallographic direction of Ag(100), and that the molecular unit cell depicted in Figure 4, can be described with the vectors \mathbf{A} and \mathbf{B}' , such as:

$$\begin{pmatrix} \mathbf{A} \\ \mathbf{B}' \end{pmatrix} = \begin{pmatrix} 5 & -2 \\ 6 & 8 \end{pmatrix} \begin{pmatrix} \mathbf{a} \\ \mathbf{b} \end{pmatrix}, \quad (2)$$

where \mathbf{a} and \mathbf{b} are in the $[011]$ and $[01\bar{1}]$ directions, respectively. \mathbf{A} and \mathbf{B}' have for dimensions 15.6 \AA and 29.0 \AA , respectively. In the absence of information regarding exact adsorption sites, if the center of tetracene is placed on a top site of the Ag(100) surface, each FM-rubrene molecules have a similar top adsorption site. This adsorption model for FM-rubrene, with two molecules per unit cell and a cell area of 434.3 \AA^2 , leads to a packing density of 4.6×10^{13} molecules per cm^2 , which, as expected for the larger molecule, is smaller than that obtained for rubrene. Here again, no STM stable images were obtained beyond one monolayer for this system.

Comparing the geometries that rubrene and FM-rubrene molecules assume when they self-assemble on the Ag(100) surface to that of their bulk crystalline structures can aid in understanding why epitaxial growth has never been achieved on such surfaces, and what might need be improved to realize epitaxial growth. Both rubrene and FM-rubrene crystallize in the orthorhombic crystal structure, the unit cell for which the rubrene is shown in Figure 5 a). Considering the (a,b) plane highlighted in Figure 5 a), and shown in detail in Figure 5 b), one can select a few relevant parameters to compare the

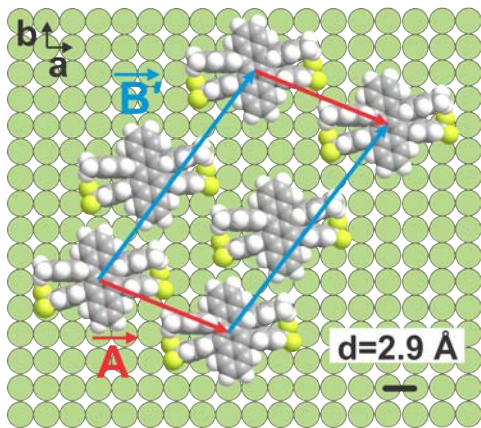


FIG. 4. Binding model for one monolayer FM-rubrene on Ag(100), determined from the STM data in figure 3. The lengths of the vectors \mathbf{A} and \mathbf{B}' are 15.6 Å and 29.0 Å, respectively. Green circles represent surface Ag atoms, which have spacing 2.9 Å. \mathbf{a} and \mathbf{b} are in the direction of vectors $[011]$ and $[01\bar{1}]$, respectively.

STM results from both molecules with their bulk properties as measured using XRD⁹. Three points of comparison are chosen: the lengths of the unit cell vectors \mathbf{A} and \mathbf{B} (as well as $\mathbf{B}'=2\mathbf{B}$), the angle θ between the vectors \mathbf{A} and \mathbf{B} , and the azimuthal angle ϕ defined as the angle between the axis of the tetracene backbone and the line bisecting \mathbf{A} and \mathbf{B} . These values are tabulated in Figure 5 c).

In the rubrene monolayer, the measured lengths of \mathbf{A} and \mathbf{B} are about 12% smaller and 6% longer, respectively, than the single crystal values. In the FM-rubrene film, the length of $2\mathbf{B}$ has been compared to \mathbf{B}' , which is defined as twice the corresponding length in the single crystal to account for the two molecules in the unit cell. The STM measurements of the lengths of \mathbf{A} and \mathbf{B}' are about 10% smaller and 17% longer, respectively, than the FM-rubrene single crystal values. Next, the angle θ between the two unit cell vectors is 56° for the rubrene monolayer vs. 29.82° for the rubrene crystal, and 74° for the FM-rubrene monolayer vs. 23.62° for the corresponding crystal. Finally, the azimuthal angle ϕ was found to be slightly increased for the rubrene monolayer (95°) with respect to single crystal rubrene (90.00°), while it is found slightly decreased for the FM-rubrene monolayer (85°) in comparison to its corresponding value in the crystal form (90.00°).

From these results, it can be seen that the tetracene twisting, typically pointed to in order to explain a lack of crystalline order in rubrene thin films, is not the only parameter preventing epitaxial growth of rubrene. The unit cell of the adsorbed rubrene is very different from its bulk counterpart. This is underscored by the behavior of the FM-rubrene monolayer. The molecules, similar to the gas phase, have a planar tetracene backbone, but the unit cell of the monolayer is so distinct from that of the bulk that epitaxial growth cannot take place.

The geometry assumed by the molecules in a self-assembled organic monolayer is often a fine balance between molecule/molecule and molecule/surface interactions. For the two molecules studied here, dispersion forces with the substrate favor tetracene backbones aligned parallel to the surface, but this is counteracted by the bulkiness of the phenyl units. Therefore, only adsorption modes resembling the stacking of the (\mathbf{a},\mathbf{b}) plane of the bulk crystal will be realized on surfaces with high polarizability. Vertical stacking of the tetracene has been observed only on ordered molecular layers, in part because the layers were C-H terminated, thereby reducing the backbone-surface dispersion forces in favor of the intermolecular dispersion forces. In some cases, the corrugation of the organic substrate was thought to provide additional stability. Therefore, stacking that exposes a (\mathbf{b},\mathbf{c}) plane can be obtained. These observations highlight several considerations that could be exploited to select a particular molecular orientations with respect to the underlying surface, and tune the monolayers unit cells to promote epitaxial growth in a desired orientation on a metallic or semiconductor substrate. For example, using a textured surface, such as a Au(100) or rutile TiO₂(110), could be used as a template, directing the order of the initial rubrene layer.⁴² Moreover, molecule-surface dispersion forces could be reduced by terminating a surface with C-F groups of very low polarizability, and therefore allow intermolecular forces to dominate the molecular self-assembly process.

B. Electronic structure and energy alignment

In this section, both the electronic structure and the energy alignment of rubrene and FM-rubrene on Ag(100) will be compared. As a reference point, however, it is useful to consider first the electronic structure of thick multilayers, measured in occupied and unoccupied states, and shown in Figure 6.

The solid curves of Figures 6 a) and b) are the secondary electron cut off (SECO) obtained from UPS, as well as the VB and CB measured using UPS and IPS, respectively, for a thick layer of rubrene molecules grown on Ag(100). For these spectra, the zero of energy is taken as the measured Fermi level and the occupied and unoccupied states are assigned negative and positive energies, respectively. For such thickness, characteristic features of the silver surface are no longer visible so that the spectra are representative of the molecular electronic structure, and compare well to the DOS calculated for a gas phase rubrene molecule, shown as the dotted line in Figure 6 b). The occupied and unoccupied states of the calculated DOS have been rigidly shifted in energy to align with their experimental counterparts. Thus the highest occupied molecular orbital (HOMO) and the lowest unoccupied molecular orbital (LUMO) can be easily found at -2.3 eV and +2.0 eV, respectively, resulting in a HOMO-LUMO gap, often considered the transport gap, of 4.3 eV.

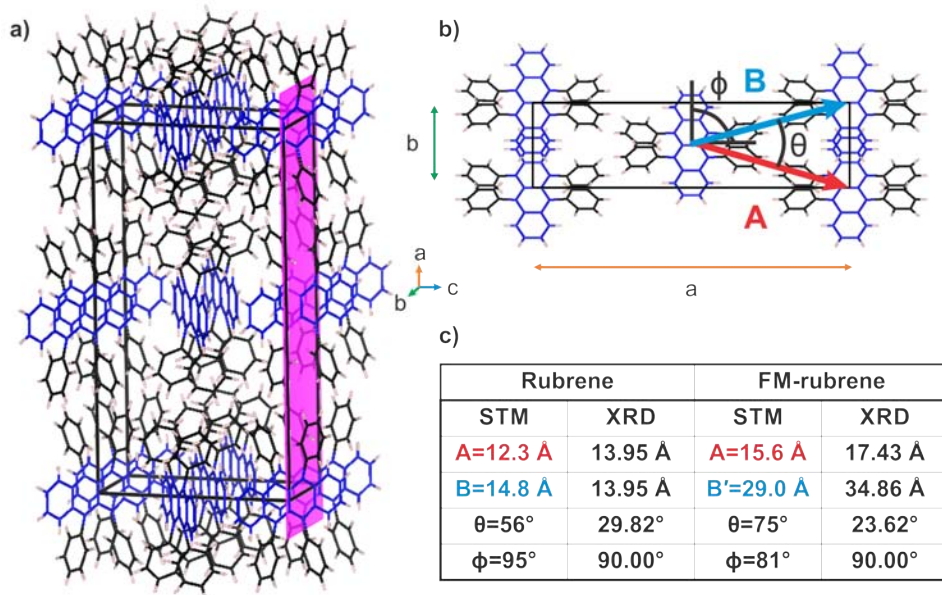


FIG. 5. Schematic representation of our comparison of STM results with literature XRD data⁹. (a) Unit cell of single crystal rubrene (and FM-rubrene, not shown) with the a-b plane indicated for clarity. (b) Two dimensional slice of an a-b plane used for comparison, with the compared surface lattice vectors, **A** and **B** labelled. (c) Table of relevant lengths and angles used.

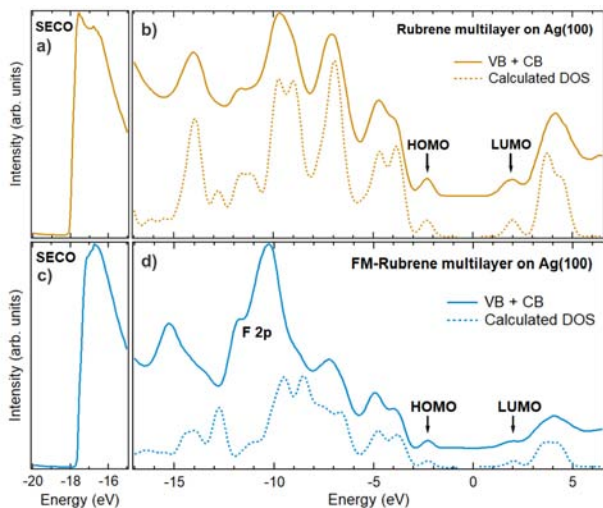


FIG. 6. (a) and (c) Secondary electron cutoffs (SECO); (b) and (d) UPS and IPS spectra (solid curves) of thick films of rubrene (b) and FM-rubrene (d) on Ag(100), each compared to the calculated DOS (dotted curves).

As shown in Figure S2, the rubrene frontier orbitals are centered on the tetracene backbone, while phenyl-related states are found at energies below the HOMO and above the LUMO. By measuring the width of the photoemission spectrum and comparing to the photon energy, an electron affinity of 1.1 eV is determined for a rubrene thick film.

A similar analysis can be performed on the spectra of Figure 6 c) and d), where the SECO, VB and CB

have been measured from a thick layer of FM-rubrene. Both occupied and unoccupied states are in good agreement with the adjusted DOS calculated for a gas phase FM-molecule shown as a dotted line, except for the -12 to -10 eV region, where the large cross section of the F 2p states is not taken into account in the DOS. The HOMO and LUMO for FM-rubrene are also measured at -2.3 eV and +2.0 eV, respectively, resulting in a gap of 4.3 eV. That rubrene and FM-rubrene have the same HOMO-LUMO gap should not be surprising, as the frontier orbitals for FM-rubrene are also found localized on its tetracene backbone as indicated in Figure S2. While the absolute energy of the HOMO and LUMO may be affected, their relative energy is not. For example, our calculations indicate a global shift of the HOMO and LUMO of FM-rubrene of ~ 0.2 eV to lower energies, compared to rubrene. This is not observed here, for a reason that will be explained later. Finally, from these measurements, an electron affinity of 1.5 eV is determined for FM-rubrene. These results are also in good agreement with reported cyclic voltammetry data.⁹

To explore both the effect of rubrene functionalization and the effect of layer thickness on the molecular orbitals alignment with respect to the substrate band structure, the SECO, VB and CB were measured on a clean Ag(100) surface and for varying thicknesses of rubrene and FM-rubrene on Ag(100) as shown in Figure 7 and Figure 8. VB and CB spectra have been normalized in intensity to the Fermi edge of Ag. As slight electron beam damage was observed during IPS, each molecular film was freshly grown on top of a clean Ag surface for a given thickness.

As seen in Figure 7 and Figure 8, the electronic struc-

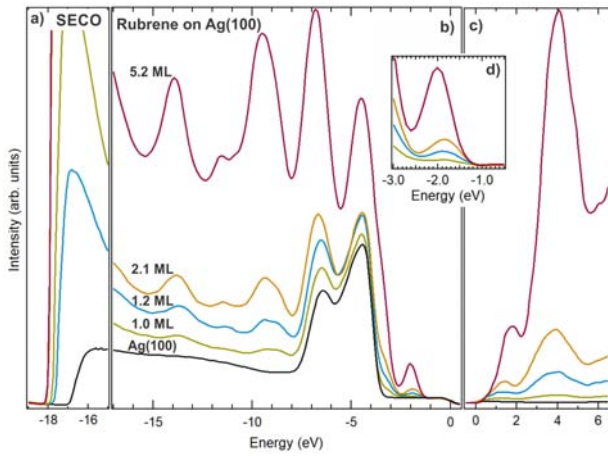


FIG. 7. a) SECO, b) UPS c) IPS spectra of the combined rubrene on Ag(100) system at varying coverages. Spectra normalized to the Ag(100) Fermi level at 0 eV. d) Zoomed-in region of the HOMO.

ture of Ag(100) is characterized by Ag 4d states found between -8 eV and -4 eV, and by a well-defined Fermi edge, both in occupied and unoccupied states, set at 0 eV. The SECO of the clean surface is found at -17.0 eV, resulting in a work function for Ag(100) or 4.2 eV, in agreement with previous work.⁴³

After deposition of 1 ML of rubrene on the Ag surface, molecular features resembling those measured on the thick rubrene layer are observed in both the occupied and unoccupied states. This indicates, consistent with our STM images, that rubrene adsorbs non-dissociatively on Ag(100). The HOMO and LUMO of 1ML rubrene are measured at -1.8 eV and 1.1 eV, respectively, resulting in a molecular gap of 2.9 eV. Upon adsorption an interface dipole of 0.7 eV develops between rubrene and the Ag surface, in good agreement with previous work.^{33,36} When further rubrene is added, the occupied molecular states (respectively, unoccupied states) are slowly pushed to more negative energies (respectively, to more positive energies), until they stabilize to the values obtained for the thick multilayer of Figure 7. The representative evolution of the HOMO is shown in the inset of Figure 7. This behavior is typical for metal surfaces, where the molecules in the first layer experience greater final state screening of the VB hole created in UPS or added electron in IPS. The energy alignment diagrams for rubrene on Ag(100), for 1 ML and for a thick multilayer, are given in Figure 9.

Qualitatively similar results are obtained for FM-rubrene deposited on Ag(100), as seen in Figure 8. The HOMO and LUMO of 1ML rubrene are measured at -2.0 eV and +0.9 eV, respectively, resulting in a molecular gap of 2.9 eV. Again, the molecular gap of FM-rubrene is similar to that of rubrene for 1ML. Assuming a molecule/surface interaction similar in magnitude to that of the rubrene/surface system, finding the FM-rubrene molecular orbitals slightly lower in energy is compatible

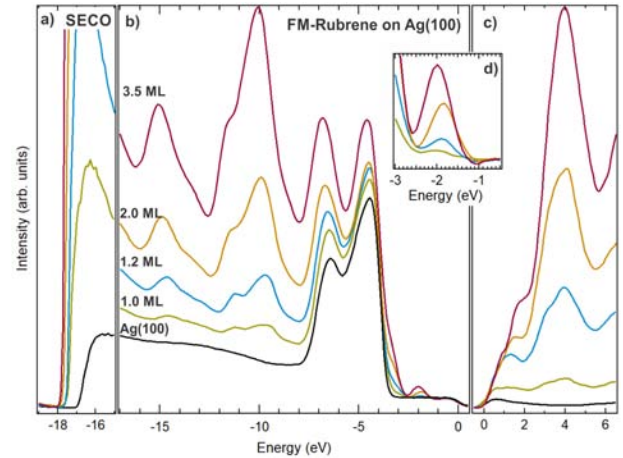


FIG. 8. a) SECO, b) UPS c) IPS spectra of the combined FM-rubrene on Ag(100) system at varying coverages. All spectra normalized to the Ag(100) Fermi level at 0 eV. d) Zoomed-in region of the HOMO.

with the calculated DOS of Figure S2. Concomitantly, an interface dipole of 0.5 eV develops between 1ML FM-rubrene and Ag(100). However, for 1.2 ML coverage, the molecular orbitals are found pushed to more positive energies by about 0.2 eV as shown in Figure 8 d). Only after that, for increasing thicknesses, the occupied and unoccupied states start shifting slowly to more negative energies due to loss of substrate screening, reaching the values obtained for a thick molecular layer. The energy alignment of 1ML and of a thick layer of FM-rubrene is summarized in Figure 9.

Although the molecular orbitals of 1ML FM-rubrene are found lower in energy than those of rubrene, for higher coverages, the frontier orbitals of both molecules are found at the same position. This can be explained as follows: FM-rubrene possesses an intrinsic dipole arising from charge transfer from the -CH₃ groups to the -CF₃ groups. Assuming that FM-rubrene adsorbs nearly-rigidly on the Ag surface and due to the larger size of -CF₃ with respect to -CH₃, the molecular dipole makes an angle of $\sim 45^\circ$ with respect to the surface normal, resulting in a small dipolar contribution along the surface normal. The long range order observed in STM, and the strict alternation of -CH₃ and -CF₃ groups, can give rise to an homogeneous dipolar contribution in the first molecular layer. Using the molecular density, $n = 4.6 \times 10^{13}$ molecules per cm², obtained from STM, the potential energy arising from the molecular dipole layer can be estimated from the formula

$$V(1 \text{ ML}) = \frac{np \sin(\alpha)}{\epsilon_0} \approx 0.2 \text{ eV}, \quad (3)$$

where p is the magnitude of the intrinsic dipole moment, 2.14 D, making an angle α with the surface normal, and where α is estimated to be $\sim 45^\circ$.

It can be argued that FM-rubrene adsorbed on weakly interacting surfaces, as long as they are smooth enough,

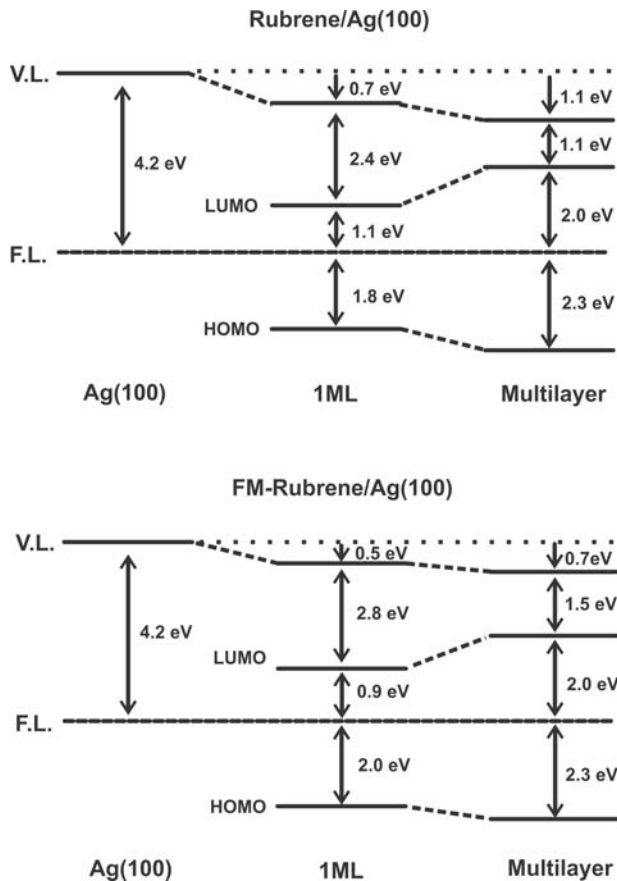


FIG. 9. Energy level alignment diagram for rubrene on Ag(100) (top) and FM-rubrene on Ag(100) (bottom). Fermi level (F.L.) and vacuum level (V.L.) are indicated for Ag(100), one monolayer coverage, and multilayer coverage, whereas HOMO and LUMO positions are indicated for monolayer and multilayer coverage.

will tends to always reproduce such $-\text{CH}_3$ and $-\text{CF}_3$ groups alternation, and therefore will most-likely give rise to a dipole layer. As a result, additional molecular lay-

ers should be affected by the presence of such dipole, and have their electronic structure rigidly shifted in energy. In particular, one can imagine a geometry where the tetracene angle with the surface plane is increased, resulting in an even stronger dipole layer. Moreover, the energy shift is present even for the disordered, multilayer FM-rubrene films measured here. This implies that the initial FM-rubrene monolayer in contact with the Ag surface remains stable and the shift it induces does not require further epitaxy. Therefore, it may be used as an interface dipole layer to shift the energy level alignment of other organic molecular layers that are subsequently deposited.

IV. CONCLUSION

The self-assembly of rubrene and FM-rubrene on Ag(100), studied at room temperature using STM, indicates long range order for monolayer coverages, with a surface packing resembling that of the (a,b) plane of single crystals. Rubrene and FM-rubrene particular geometries on Ag(100), are favored by strong dispersion forces between the polarizable metal surface and the tetracene backbones, leading to a flat adsorption of the tetracenes mitigated by the bulkiness of the pendant phenyl groups. In such configurations, both for rubrene and FM-rubrene, distortions of the unit cell prevent the epitaxial growth of additional layers. It is proposed that surface passivation with weakly polarizable groups could reduce molecule/surface interaction, favor molecule/molecule interactions, and lead to more bulk-like geometries.

In the case of FM-rubrene, the strict alternation of the $-\text{CH}_3$ and $-\text{CF}_3$ groups within the molecular layer and the presence of an intrinsic molecular dipole, lead to an homogeneous dipole layer at the surface of Ag(100). Consequently, the energy levels of additional molecular layers are shifted in energy by 0.2 eV. As the dipole strength depends on the position of electron donating and electron withdrawing groups, and on the resulting adsorption geometry, larger dipoles could be achieved for other fluorine-functionalized rubrene molecules.

¹ V. Podzorov, E. Menard, A. Borissov, V. Kiryukhin, J. A. Rogers, and M. E. Gershenson, *Phys. Rev. Lett.* **93**, 086602 (2004).

² M. E. Gershenson, V. Podzorov, and A. F. Morpurgo, *Rev. Mod. Phys.* **78**, 973 (2006).

³ M. F. Calhoun, J. Sanchez, D. Olaya, M. E. Gershenson, and V. Podzorov, *Nature Materials* **7**, 84 (2007).

⁴ H. Alves, A. S. Molinari, H. Xie, and A. F. Morpurgo, *Nature Materials* **7**, 574 (2008).

⁵ H. Alves, R. M. Pinto, and E. S. Maçôas, *Nature Communications* **4**, 1842 (2013).

⁶ R. M. Pinto, E. M. S. Macoas, and H. Alves, *J. Mater. Chem. C* **2**, 3639 (2014).

⁷ daSilvaFilho D.A., K. E.G., and B. J.L., *Advanced Materials* **17**, 1072,

<https://onlinelibrary.wiley.com/doi/pdf/10.1002/adma.200401866>.

⁸ V. Coropceanu, H. Li, P. Winget, L. Zhu, and J.-L. Brédas, *Annual Review of Materials Research* **43**, 63 (2013), <https://doi.org/10.1146/annurev-matsci-071312-121630>.

⁹ K. A. McGarry, W. Xie, C. Sutton, C. Risko, Y. Wu, V. G. Young Jr, J.-L. Brédas, C. D. Frisbie, and C. J. Douglas, *Chemistry of Materials* **25**, 2254 (2013).

¹⁰ W. A. Ogden, S. Ghosh, M. J. Bruzek, K. A. McGarry, L. Balhorn, V. Young Jr, L. J. Purvis, S. E. Wegwerth, Z. Zhang, N. A. Serratore, *et al.*, *Crystal Growth & Design* **17**, 643 (2017).

¹¹ H. Ma, N. Liu, and J.-D. Huang, *Scientific reports* **7**, 331 (2017).

¹² W. Xie, P. L. Prabhumirashi, Y. Nakayama, K. A. Mc-

- Garry, M. L. Geier, Y. Uragami, K. Mase, C. J. Douglas, H. Ishii, M. C. Hersam, and C. D. Frisbie, *ACS Nano* **7**, 10245 (2013), <https://doi.org/10.1021/nn4045694>.
- ¹³ D. Käfer, L. Ruppel, G. Witte, and C. Wöll, *Physical review letters* **95**, 166602 (2005).
- ¹⁴ M.-C. Blüm, E. Čavar, M. Pivetta, F. Patthey, and W.-D. Schneider, *Angewandte Chemie International Edition* **44**, 5334 (2005), <https://onlinelibrary.wiley.com/doi/pdf/10.1002/anie.200501467>.
- ¹⁵ M.-C. Blüm, M. Pivetta, F. Patthey, and W.-D. Schneider, *Physical Review B* **73**, 195409 (2006).
- ¹⁶ M. Pivetta, M.-C. Blüm, F. Patthey, and W.-D. Schneider, *Angewandte Chemie International Edition* **47**, 1076 (2008).
- ¹⁷ J. A. Miwa, F. Cicaira, S. Bedwani, J. Lipton-Duffin, D. F. Perepichka, A. Rochefort, and F. Rosei, *The Journal of Physical Chemistry C* **112**, 10214 (2008), <https://doi.org/10.1021/jp802762q>.
- ¹⁸ M. Pivetta, M.-C. Blüm, F. Patthey, and W.-D. Schneider, *ChemPhysChem* **11**, 1558 (2010), <https://onlinelibrary.wiley.com/doi/pdf/10.1002/cphc.200900846>.
- ¹⁹ F. Cicaira, J. A. Miwa, D. F. Perepichka, and F. Rosei, *The Journal of Physical Chemistry A* **111**, 12674 (2007), pMID: 17983212, <https://doi.org/10.1021/jp076090c>.
- ²⁰ M. Campione, *J. Phys. Chem. C* **112**, 16178 (2008).
- ²¹ M. Campione, M. Moret, L. Raimondo, and A. Sassella, *The Journal of Physical Chemistry C* **113**, 20927 (2009), <https://doi.org/10.1021/jp905752r>.
- ²² E. Fumagalli, M. Campione, L. Raimondo, A. Sassella, M. Moret, L. Barba, and G. Arrighetti, *Journal of Synchrotron Radiation* **19**, 682 (2012).
- ²³ S. Trabattoni, L. Raimondo, M. Campione, D. Braga, V. C. Holmberg, D. J. Norris, M. Moret, A. Ciavatti, B. Fraboni, and A. Sassella, *Advanced Materials Interfaces* **2**, 1500423 (2015), <https://onlinelibrary.wiley.com/doi/pdf/10.1002/admi.201500423>.
- ²⁴ M. Haemori, J. Yamaguchi, S. Yaginuma, K. Itaka, and H. Koinuma, *Japanese Journal of Applied Physics* **44**, 3740 (2005).
- ²⁵ W.-S. Hu, S.-Z. Weng, Y.-T. Tao, H.-J. Liu, and H.-Y. Lee, *Organic Electronics* **9**, 385 (2008).
- ²⁶ L. Raimondo, E. Fumagalli, M. Moret, M. Campione, A. Borghesi, and A. Sassella, *The Journal of Physical Chemistry C* **117**, 13981 (2013), <https://doi.org/10.1021/jp402136f>.
- ²⁷ H. Chang, W. Li, H. Tian, Y. Geng, H. Wang, D. Yan, and T. Wang, *Organic Electronics* **20**, 43 (2015).
- ²⁸ C.-H. Lee, T. Schiros, E. J. G. Santos, B. Kim, K. G. Yager, S. J. Kang, S. Lee, J. Yu, K. Watanabe, T. Taniguchi, J. Hone, E. Kaxiras, C. Nuckolls, and P. Kim, *Advanced Materials* **26**, 2812 (2014), <https://onlinelibrary.wiley.com/doi/pdf/10.1002/adma.201304973>.
- ²⁹ M. Lan, Z.-H. Xiong, G.-Q. Li, T.-N. Shao, J.-L. Xie, X.-F. Yang, J.-Z. Wang, and Y. Liu, *Physical Review B* **83**, 195322 (2011).
- ³⁰ C. G. W., D. A. R., H. L. M., D. D. A., and G. R. H., *Angewandte Chemie International Edition in English* **36**, 248 (1997), <https://onlinelibrary.wiley.com/doi/pdf/10.1002/anie.199702481>.
- ³¹ G. W. Coates, A. R. Dunn, L. M. Henling, J. W. Ziller, E. B. Lobkovsky, and R. H. Grubbs, *Journal of the American Chemical Society* **120**, 3641 (1998), <https://doi.org/10.1021/ja974072a>.
- ³² Y. L. Huang, H. Li, J. Ma, H. Huang, W. Chen, and A. T. S. Wee, *Langmuir* **26**, 3329 (2010), pMID: 20175573, <https://doi.org/10.1021/la9030798>.
- ³³ H. Ding and Y. Gao, in *Organic Field-Effect Transistors IX*, Vol. 7778 (International Society for Optics and Photonics, 2010) p. 77780J.
- ³⁴ Y. Nakayama, Y. Uragami, S. Machida, K. R. Koswattage, D. Yoshimura, H. Setoyama, T. Okajima, K. Mase, and H. Ishii, *Applied Physics Express* **5**, 111601 (2012).
- ³⁵ S. Sinha and M. Mukherjee, *Journal of Applied Physics* **114**, 083709 (2013).
- ³⁶ S. Sinha and M. Mukherjee, *AIP Advances* **5**, 107204 (2015).
- ³⁷ F. Anger, H. Glowatzki, A. Franco-Cañellas, C. Bürker, A. Gerlach, R. Scholz, Y. Sakamoto, T. Suzuki, N. Koch, and F. Schreiber, *The Journal of Physical Chemistry C* **119**, 6769 (2015).
- ³⁸ I. Horcas, R. Fernández, J. M. Gómez-Rodríguez, J. Colchero, J. Gómez-Herrero, and A. M. Baro, *Review of Scientific Instruments* **78**, 013705 (2007), <https://doi.org/10.1063/1.2432410>.
- ³⁹ E. Bersch, S. Rangan, R. A. Bartynski, E. Garfunkel, and E. Vescovo, *Phys. Rev. B* **78**, 085114 (2008).
- ⁴⁰ D. Arena, F. Curti, and R. Bartynski, *Surface Science* **369**, L117 (1996).
- ⁴¹ M. W. Schmidt, K. K. Baldrige, J. A. Boatz, S. T. Elbert, M. S. Gordon, J. H. Jensen, S. Koseki, N. Matsunaga, K. A. Nguyen, S. Su, T. L. Windus, M. Dupuis, and J. A. Montgomery, *Journal of Computational Chemistry* **14**, 1347 (1993), <https://onlinelibrary.wiley.com/doi/pdf/10.1002/jcc.540141112>.
- ⁴² J. de la Figuera, M. A. González, R. García-Martínez, J. M. Rojo, O. S. Hernán, A. L. V. de Parga, and R. Miranda, **58**, 1169 (1998).
- ⁴³ M. Chelvayohan and C. Mee, *Journal of Physics C: Solid State Physics* **15**, 2305 (1982).